

5 Aliasing Artifacts and Noise in CT Images

The errors discussed in the last chapter are fundamental to the projection process and depend upon the interaction of object inhomogeneities with the form of energy used. The effects of these errors can't be lessened by simply increasing the number of measurements in each projection or the total number of projections.

This chapter will focus on reconstruction errors of a different type: those caused either by insufficiency of data or by the presence of random noise in the measurements. An insufficiency of data may occur either through undersampling of projection data or because not enough projections are recorded. The distortions that arise on account of insufficiency of data are usually called the aliasing distortions. Aliasing distortions may also be caused by using an undersampled grid for displaying the reconstructed image.

5.1 Aliasing Artifacts

We will discuss aliasing from two points of view. First we will assume point sources and detectors and show the artifacts due to aliasing. With this assumption it is easy to show the effects of undersampling a projection, using too small a number of views, and choosing an incorrect reconstruction grid or filter. We will then introduce detectors and sources of nonzero width and discuss how they in effect help reduce the severity of aliasing distortions.

5.1.1 What Does Aliasing Look Like?

Fig. 5.1 shows 16 parallel beam reconstructions of an ellipse with various values of K , the number of projections, and N , the number of rays in each projection. The projections for the ellipse were generated as described in Chapter 3. The gray level inside the ellipse was 1 and the background 0 and the data were generated assuming a point source and point detector. To bring out all the artifacts, the reconstructed images were windowed between 0.1 and -0.1 . (In other words, all the gray levels above 0.1 were set at white and all below -0.1 at black.) The images in Fig. 5.1 are displayed on a 128×128 matrix. Fig. 5.2 is a graphic depiction of the reconstructed numerical values on the middle horizontal lines for two of the images in Fig. 5.1. From

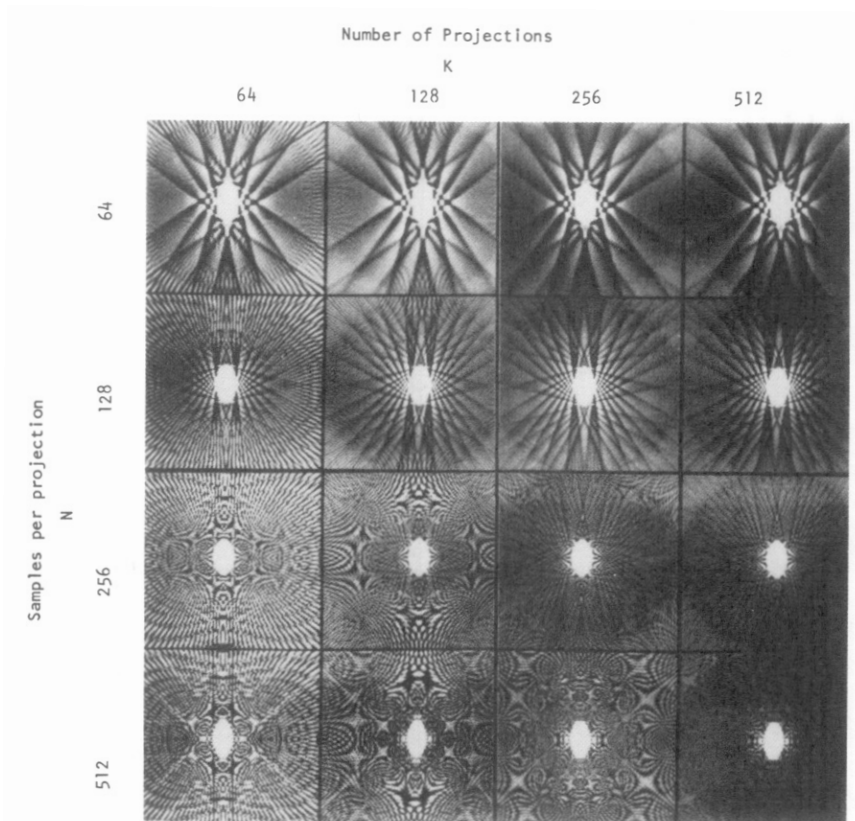


Fig. 5.1: Sixteen reconstructions of an ellipse are shown for different values of K , the number of projections, and N , the number of rays in each projection. In each case the reconstructions were windowed to emphasize the distortions. (Courtesy of Carl Crawford of the General Electric Medical Systems Division in Milwaukee, WI.)

Figs. 5.1 and 5.2 the following artifacts are evident: Gibbs phenomenon, streaks, and Moiré patterns.

We will now show that the streaks evident in Fig. 5.1 for the cases when N is small and K is large are caused by aliasing errors in the projection data. Note that a fundamental problem with tomographic images in general is that the objects (in this case an ellipse), and therefore their projections, are not bandlimited. In other words, the bandwidth of the projection data exceeds the highest frequency that can be recorded at a given sampling rate. To illustrate how aliasing errors enter the projection data assume that the Fourier transform $S_\theta(f)$ of a projection $P_\theta(t)$ looks as shown in Fig. 5.3(a). The bandwidth of this function is B as also shown there. Let's choose a sampling interval τ for sampling the projection. By the discussion in Chapter 2, with this sampling interval we can associate a measurement bandwidth W which is equal to $1/2\tau$. We will assume that $W < B$. It follows that the Fourier transform of the *samples* of the projection data is given by Fig. 5.3(b). We see that the information within the measurement band is contaminated by the tails (shaded areas) of the higher and lower replications of the original Fourier transform. This contaminating information constitutes the aliasing

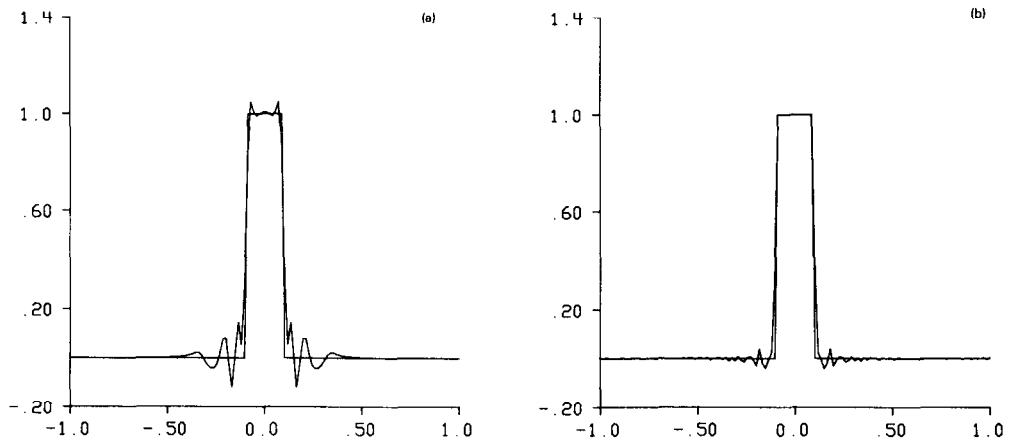


Fig. 5.2: The center lines of the reconstructions shown in Fig. 5.1 for (a) $N = 64$, $K = 512$ and (b) $N = 512$, $K = 512$ are shown here. (From [Cra79].)

errors in the sampled projection data. These contaminating frequencies constitute the aliased spectrum.

Backprojection is a linear process so the final image can be thought to be made up of two functions. One is the image made from the bandlimited projections degraded primarily by the finite number of projections. The second is the image made from the aliased portion of the spectrum in each projection.

The aliased portion of the reconstruction can be seen by itself by subtracting the transforms of the sampled projections from the corresponding theoretical transforms of the original projections. Then if this result is filtered as before, the final reconstructed image will be that of the aliased spectrum. We performed a computer simulation study along these lines for an elliptical object. In order to present the result of this study we first show in Fig. 5.4(a) the reconstruction of the ellipse for $N = 64$. (The number of projections was 512, which is large enough to preclude any artifacts due to insufficient number of views, and will remain the same for the discussion here.) We have subtracted the transform of each projection for the $N = 64$ case from the corresponding transform for the $N = 1024$ case. The latter was assumed to be the true transform because the projections are oversampled (at least in comparison to the $N = 64$ case). The reconstruction obtained from the difference data is shown in Fig. 5.4(b). Fig. 5.4(c) is the bandlimited image obtained by subtracting the aliased-spectrum image of Fig. 5.4(b) from the complete image shown in Fig. 5.4(a). Fig. 5.4(c) is the reconstruction that would be obtained provided the projection data for the $N = 64$ case were truly bandlimited (i.e., did not suffer from aliasing errors after sampling). The aliased-spectrum reconstruction in Fig. 5.4(b) and the absence of streaks in Fig. 5.4(c) prove our point that when the number of projections is large, the streaking artifacts are caused by aliasing errors in the projection data.

We will now present a plausible argument, first advanced by Brooks *et al.*

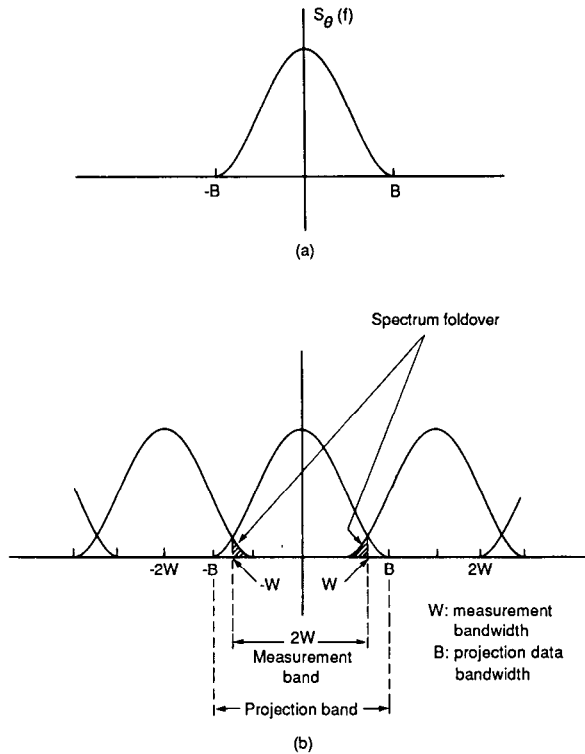


Fig. 5.3: *If a projection (a) is sampled at below the Nyquist rate ($2B$ in this case), then aliasing will occur. As shown in (b) the result is aliasing or spectrum foldover. (Adapted from [Cra79].)*

[Bro79], for when a streak may be dark and when it may be light. Note that when an object is illuminated by a source, a projection of the object is formed at the detector array as shown in Fig. 5.5. If the object has a discontinuity at its edges, then the projection will also. We will now show how the position of this discontinuity with respect to the detector array has a bearing on the sign of the aliasing error. When the filtered projection is backprojected over the image array the sign of the error will determine the shade of the streak.

Consider sampling a projection described by

$$f(x) = \begin{cases} 1 & x > 0 \\ -1 & \text{elsewhere.} \end{cases} \quad (1)$$

The Fourier transform of this function is given by

$$F(\omega) = \frac{-2j}{\omega}. \quad (2)$$

For the purpose of sampling, we can imagine that the function f is multiplied by the function

$$h(x) = \sum_{k=-\infty}^{\infty} \delta(x - kT) \quad (3)$$

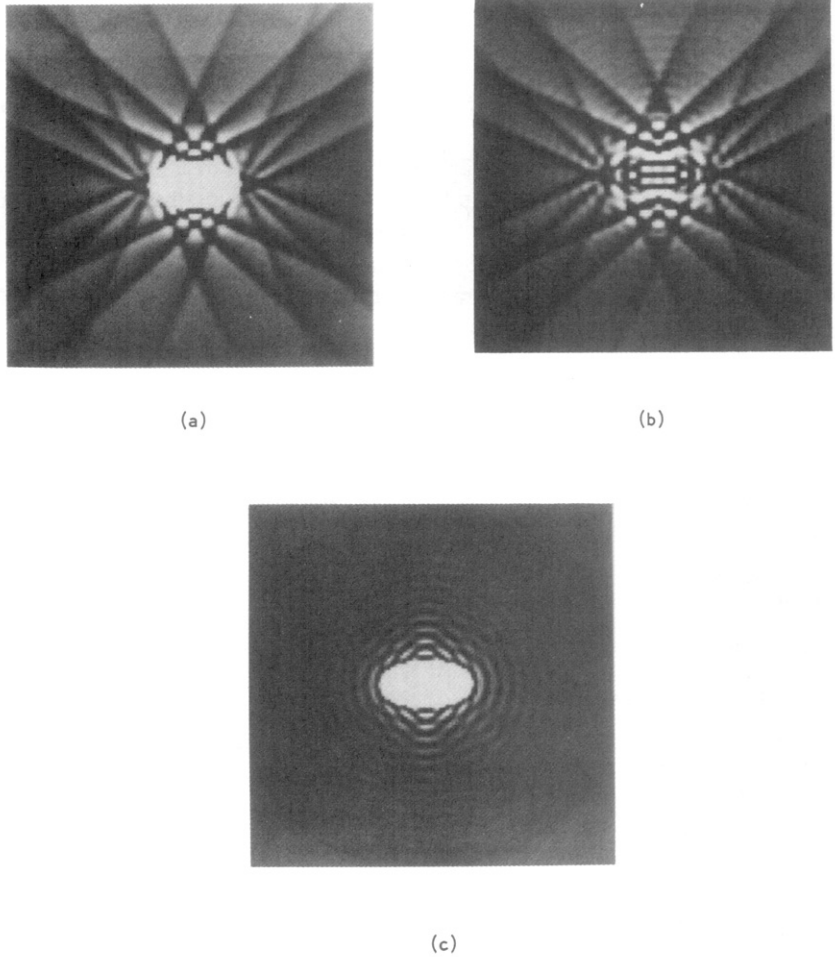


Fig. 5.4: (a) Reconstruction of an ellipse with $N = 64$ and $K = 512$. (b) Reconstruction from only the aliased spectrum. Note that the streaks exactly match those in (a). (c) Image obtained by subtracting (b) from (a). This is the reconstruction that would be obtained provided the data for the $N = 64$ case were truly bandlimited. (From [Cra79].)

where T represents the sampling interval of the projection. The Fourier transform of the sampling function is then given by

$$H(\omega) = \sum_{k=-\infty}^{\infty} \delta(\omega - k\omega_N) \quad (4)$$

where $\omega_N = 2\pi/T$. Clearly, the Fourier transform of the sampled function is a convolution of the expressions in (2) and (4):

$$F_{\text{sampled}}(\omega) = \sum_{k=-\infty}^{\infty} \frac{-2j}{\omega + k\omega_N}. \quad (5)$$

This function is shown in Fig. 5.6(a). Before these projection data can be backprojected they must be filtered by multiplying the Fourier transform of

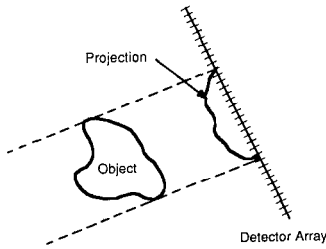


Fig. 5.5: The projection of an object with sharp discontinuities will have significant high frequency energy.

the projection by $|\omega|/2\pi$. The filtered projection is then written

$$F'_{\text{sampled}}(\omega) = \sum_{k=-\infty}^{\infty} \frac{|\omega|}{2\pi} \frac{-2j}{\omega + k\omega_N} \quad (6)$$

To study the errors due to aliasing, we will only consider the terms for $k = 1$ and $k = -1$, and assume that the higher order terms are negligible. Note that the zeroth order term is the edge information and is part of the desired reconstruction; the higher order terms are part of the error but will be small compared to the $k = \pm 1$ terms at low frequencies. The inverse Fourier transform of these two aliased terms is written as

$$f_{\text{error}}(x) \approx \frac{1}{2\pi} \int_{-\omega_N/2}^{\omega_N/2} \frac{|\omega|}{2\pi} \left[\frac{-2j}{\omega + \omega_N} + \frac{-2j}{\omega - \omega_N} \right] e^{-j\omega x} d\omega \quad (7)$$

and is shown in Fig. 5.6(b).

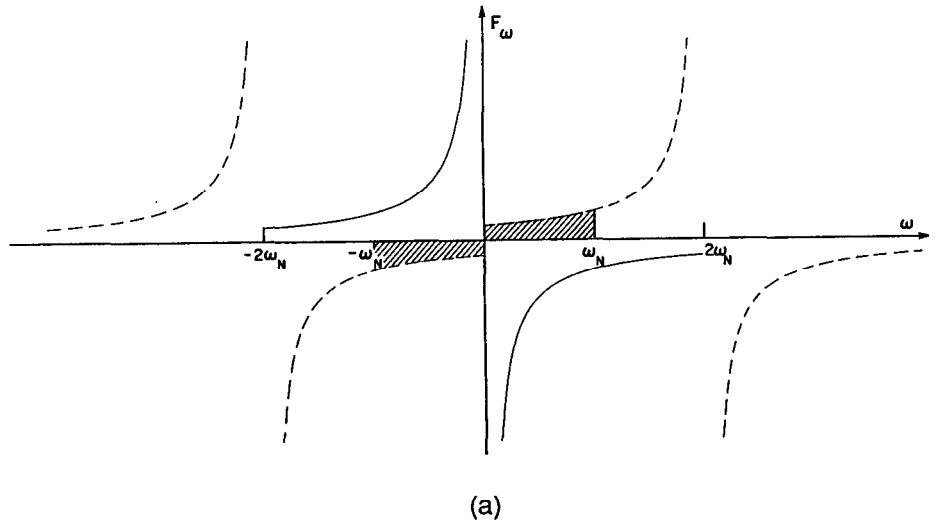
Now if the sampling grid is shifted by 1/4 of the sampling interval its Fourier transform is multiplied by $e^{+jk\omega_N(T/4)}$ or

$$F_{\text{shifted}}(\omega) = \sum_{k=-\infty}^{\infty} \frac{|\omega|}{2\pi} \frac{-2j}{\omega + k\omega_N} e^{jk\omega_N(T/4)} \quad (8)$$

This can be evaluated for the $k = 1$ and $k = -1$ terms to find the error integral is

$$f_{\text{shifted}}(x) \approx \frac{1}{2\pi} \int_{-\omega_N/2}^{\omega_N/2} \frac{|\omega|}{2\pi} \left[\frac{2}{\omega + \omega_N} - \frac{2}{\omega - \omega_N} \right] e^{-j\omega x} d\omega \quad (9)$$

Fig. 5.6: The aliasing due to undersampled projections is illustrated here. (a) shows the Fourier transform of an edge discontinuity. The aliased portions of the spectrum are shaded. (b) shows an approximation to the error when the sampling grid is aligned with the discontinuity and (c) shows the error when the discontinuity is shifted by 1/4 of the sampling interval. Note the magnitude of the error changes by more than a factor of 3 when the sampling grid shifts.



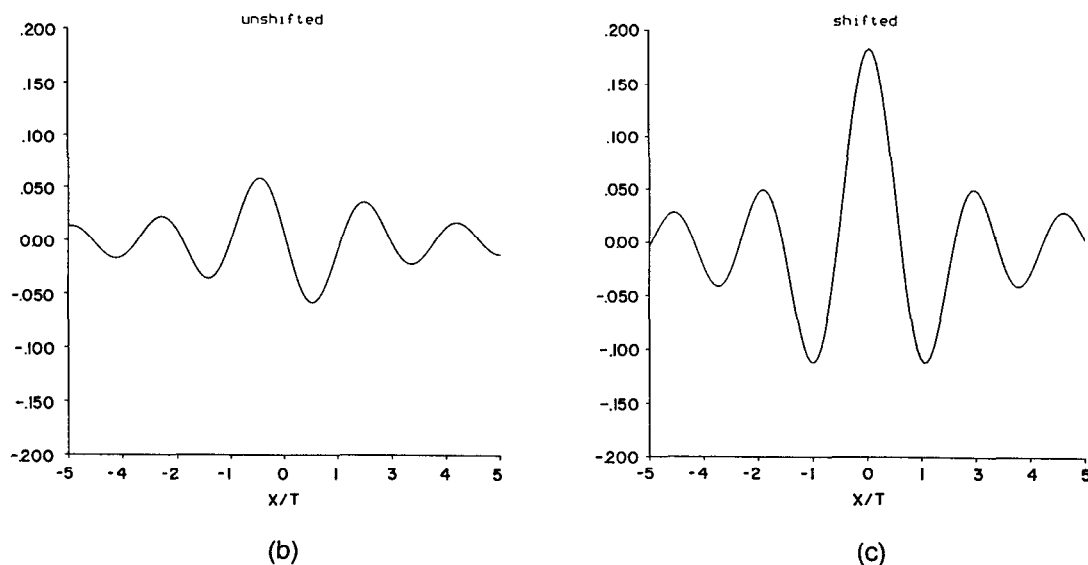
and is shown in Fig. 5.6(c). If the grid is shifted in the opposite direction, then the error will be similar but with the opposite sign.

As was done earlier in this section, consider the sampled projection to consist of two components: the true projection and the error term. The true projection data from each view will combine to form the desired image; the error in each projection will combine to form an image like that in Fig. 5.4(b). A positive error in a projection causes a light streak when the data are backprojected. Likewise, negative errors lead to dark streaks. As the view angle changes the size of the ellipse's "shadow" changes and the discontinuity moves with respect to the detector array. In addition, where the curvature of the object is large, the edge of the discontinuity will move rapidly which results in a large number of streaks.

The thin streaks that are evident in Fig. 5.1 for the cases of large N and small K (e.g., when $N = 512$ and $K = 64$) are caused by an insufficient number of projections. It is easily shown that when only a small number of filtered projections of a small object are backprojected, the result is a star-shaped pattern. This is illustrated in Fig. 5.7: in (a) are shown four projections of a point object, in (b) the filtered projections, and in (c) their backprojections.

The number of projections should be roughly equal to the number of rays in each projection. This can be shown analytically for the case of parallel projections by the following argument: By the Fourier Slice Theorem, the Fourier transform of each projection is a slice of the two-dimensional Fourier transform of the object. In the frequency domain shown in Fig. 5.8, each radial line, such as A_1A_2 , is generated by one projection. If there are M_{proj}

Fig. 5.6: Continued.



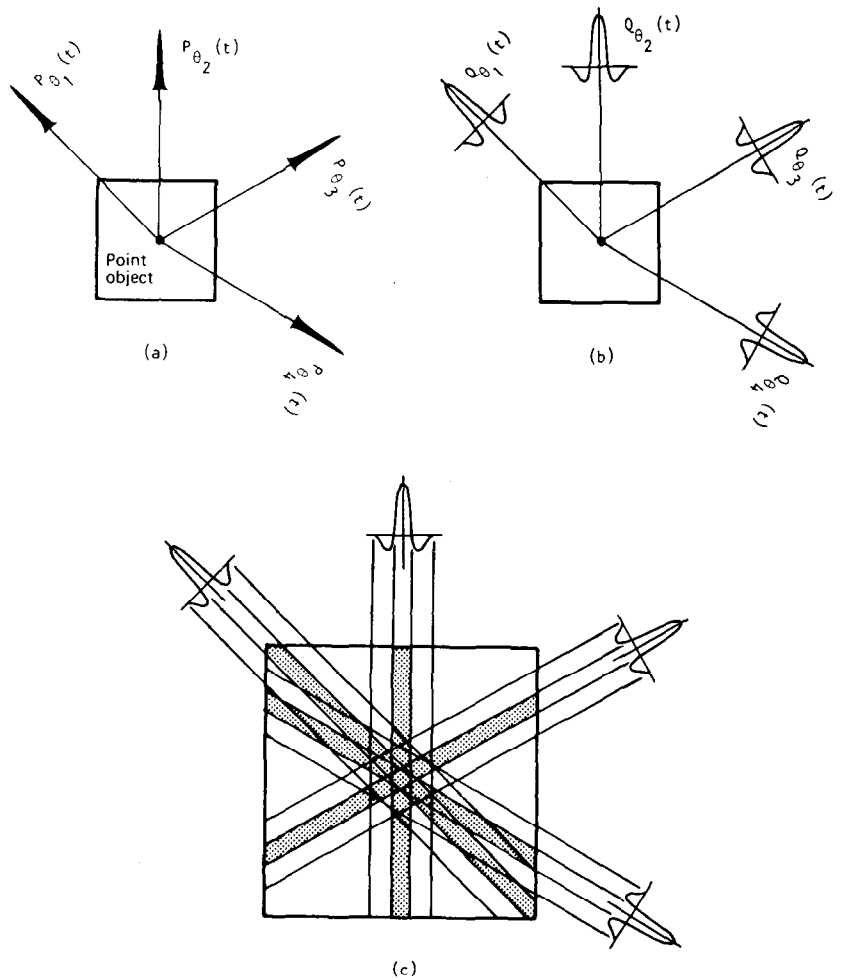


Fig. 5.7: The backprojection operation introduces a star-shaped pattern to the reconstruction. (From [Ros82].)

projections uniformly distributed over 180° , the angular interval δ between successive radial lines is given by

$$\delta = \frac{\pi}{M_{\text{proj}}} . \quad (10)$$

If τ is the sampling interval used for each projection, the highest spatial frequency W measured for each projection will be

$$W = 1/2\tau . \quad (11)$$

This is the radius of the disk shown in Fig. 5.8. The distance between consecutive sampling points on the periphery of this disk is equal to $\overline{A_2B_2}$ and

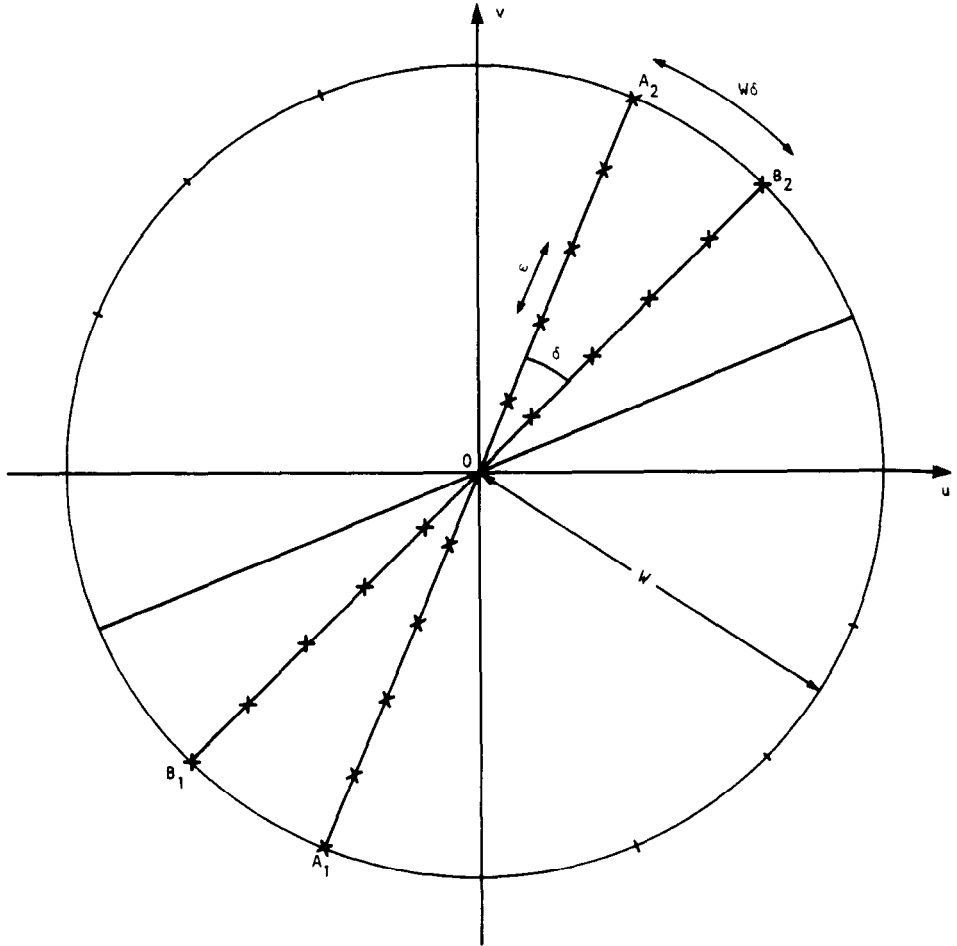


Fig. 5.8: Frequency domain parameters pertinent to parallel projection data. (From [Kak84].)

is given by

$$\overline{A_2 B_2} = W\delta = \frac{1}{2\tau} \frac{\pi}{M_{\text{proj}}} . \quad (12)$$

If there are N_{ray} sampling points in each projection, the total number of independent frequency domain sampling points on a line such as $A_1 A_2$ will also be the same. Therefore, the distance ϵ between any two consecutive sampling points on each radial line in Fig. 5.8 will be

$$\epsilon = \frac{2W}{N_{\text{ray}}} = \frac{1}{\tau N_{\text{ray}}} . \quad (13)$$

Because in the frequency domain the worst-case azimuthal resolution should

be approximately the same as the radial resolution, we must have

$$\frac{1}{2\tau} \frac{\pi}{M_{\text{proj}}} \approx \frac{1}{\tau N_{\text{ray}}}, \quad (14)$$

which is obtained by equating (12) and (13). Equation (14) reduces to

$$\frac{M_{\text{proj}}}{N_{\text{ray}}} \approx \frac{\pi}{2}, \quad (15)$$

which implies that the number of projections should be roughly the same as the number of rays per projection.

The reader may have noticed that the thin streaks caused by an insufficient number of projections (see, e.g., the image for $N = 512$ and $K = 64$ in Fig. 5.1) appear broken. This is caused by two-dimensional aliasing due to the display grid being only 128×128 . When, say, $N = 512$, the highest frequency in each projection can be 256 cycles per projection length, whereas the highest frequency that can be displayed on the image grid is 64 cycles per image width (or height). The effect of this two-dimensional aliasing is very pronounced in the left three images for the $N = 512$ row and the left two images for the $N = 256$ row in Fig. 5.1. As mentioned in Chapter 2, the artifacts generated by this two-dimensional aliasing are called Moiré patterns. These artifacts can be diminished by tailoring the bandwidth of the reconstruction kernel (filter) to match the display resolution.

From the computer simulation and analytical results presented in this section, one can conclude that for a well-balanced $N \times N$ reconstructed image, the number of rays in each projection should be roughly N and the total number of projections should also be roughly N .

5.1.2 Sampling in a Real System

In the previous section we described aliasing errors caused by undersampling the projections, number of views, and the reconstruction grid. In practice, these errors are somewhat mitigated by experimental considerations like the size of the detector aperture and the nonzero size of the x-ray source. Both these factors bring about a certain smoothing of the projections, and a consequent loss of information at the highest frequencies. In this section, we will demonstrate how these factors can be taken into account to determine the “optimum rate” at which a projection should be sampled.

In order to analyze the effect of a nonzero size for the detector aperture, note that this effect can be taken into account by convolving the ideal projection with the aperture function. Let the following function represent an aperture that is T_d units wide (we are only considering aperture widths along the projection, the width along the perpendicular direction being irrelevant to

our discussion):

$$a(x) = \begin{cases} 1 & |x| \leq \frac{T_d}{2} \\ 0 & \text{elsewhere.} \end{cases} \quad (16)$$

The Fourier transform of this aperture function is given by

$$A(\omega) = T_d \operatorname{sinc}(\omega T_d/2). \quad (17)$$

In the frequency domain, the Fourier transform of the ideal projection is multiplied by this function, implying that we are in effect passing the projection through a low pass filter (LPF). Since the first zero of $A(\omega)$ is located at $2\pi/T_d$, it is not unreasonable to say that the effect of $A(\omega)$ is to filter out all frequencies higher than

$$\omega_{\text{LPF}} = \frac{2\pi}{T_d}. \quad (18)$$

In other words, we are approximating the aperture function in the frequency domain by

$$A'(\omega) = \begin{cases} T_d \operatorname{sinc}(\omega T_d/2) & |\omega| < \omega_{\text{LPF}} \\ 0 & \text{elsewhere.} \end{cases} \quad (19)$$

Let's say that we are using an array of detectors to measure a projection and that the array is characterized by T_s as the center-to-center spacing between the detectors. Measurement of the projection data is equivalent to multiplication of the low pass filtered projection with a train $d(x)$ of impulses, where $d(x)$ is given by

$$d(x) = \sum_{n=-\infty}^{\infty} \delta(x - nT_s) \quad (20)$$

whose Fourier transform is

$$D(\omega) = \frac{2\pi}{T_s} \sum_{n=-\infty}^{\infty} \delta\left(\omega - \frac{2\pi n}{T_s}\right). \quad (21)$$

In the frequency domain the effect of the detector aperture and sampling distance is shown in Fig. 5.9. We can now write the following expression for the recorded samples p_n of an ideal projection $p(x)$:

$$p_n = \delta(x - nT_s)[p(x)*a(x)] \quad (22)$$

or, equivalently,

$$p_n = \text{IFT} \{D(\omega)*[P(\omega)A'(\omega)]\} \quad (23)$$

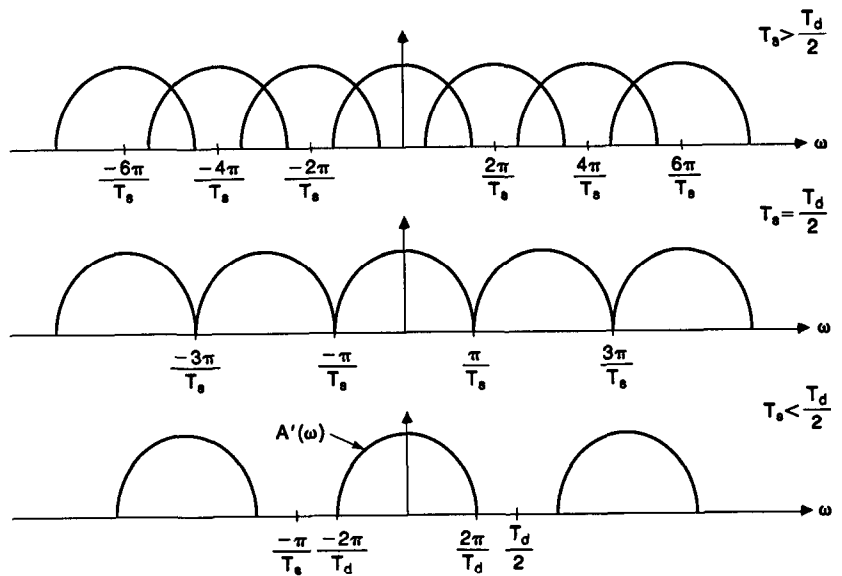


Fig. 5.9: The Fourier transform of the detector array response is shown for three different detector spacings. For values of T_s such that $T_s > T_d/2$ there will be aliasing. If $T_s \leq T_d/2$, then aliasing is minimized.

where $P(\omega)$ is the Fourier transform of the projection data and IFT is the inverse Fourier transform. Clearly, there will be aliasing in the sampled projections unless

$$T_s < \frac{T_d}{2}. \quad (24)$$

This relationship implies that we should have at least two samples per detector width [Jos80a].

There are several ways to measure multiple samples per detector width. With first-generation (parallel beam) scanners, it is simply a matter of sampling the detectors more often as the source-detector combination moves past the object. Increasing the sampling density can also be done in fourth-generation (fixed-detector) scanners by considering each detector as the apex of a fan. Now as the source rotates, each detector measures ray integrals and the ray density can be made arbitrarily dense by increasing the sampling rate for each detector.

For third-generation scanners a technique known as quarter detector offset is used. Recall that for a fan beam scanner only data for 180° plus the width of the fan need be collected; if a full 360° of data is collected then the rest of the data is effectively redundant. But if the detector array is offset by $1/4$ of the detector spacing (ordinarily, the detector bank is symmetric with respect to the line joining the x-ray source and the center of rotation; by offset is meant translating the detector bank to the left or right, thereby causing rays in opposite views to be unique) and a full 360° of data is collected it is possible to use the extra views to obtain unique information about the object. This

effectively doubles the projection sampling frequency. Fig. 5.10 compares the effect of quarter detector offset on a first-generation and a third-generation scanner.

We will now discuss the second factor that causes projections to become blurred, namely, the size of the x-ray beam. As we will show, we can't account for the extent of blurring caused by this effect in as elegant a manner as we did for the detector aperture. The primary source of difficulty is that objects undergo different amounts of blurring depending upon how far away they are from the source of x-rays. Fig. 5.11 shows the effect of a source of nonzero width. As is evident from the figure, the effect on a projection is dependent upon where the object is located between the source and the detectors.

Simple geometrical arguments show that for a given point in the object, the size of its image at the detector array is given by

$$B_s = w_s \frac{D_d}{D_s} \quad (25)$$

where w_s is the width of the source and D_d and D_s are, respectively, the distances from the point in the object to the detectors and the source. This then would roughly be a measure of blurring introduced by a nonzero-width source in a parallel beam machine.

In a fan beam system, the above-mentioned blurring is exacerbated by the natural divergence of the fan. To illustrate our point, consider two detector lines for a fan beam system, as shown in Fig. 5.12. The projection data measured along the two lines would be identical except for stretching of the projection function along the detector arc as we go to the array farther away from the center. This stretch factor is given by (see Fig. 5.13)

$$\frac{D_s}{D_s + D_d} \quad (26)$$

where the distances D_s and D_d are for object points at the center of the scan. If we combine the preceding two equations, we obtain for a fan beam system the blurring caused by a nonzero-width source

$$B_s = w_s \frac{D_d}{D_s} \frac{D_s}{D_s + D_d} = w_s \frac{D_d}{D_s + D_d} \quad (27)$$

with the understanding that, rigorously speaking, this equation is only valid for object points close to the center of rotation.

Since the size of the image is dependent on the position along the ray integral this leads to a spatially varying blurring of the projection data. Near the detector the blurring will be small while near the source a point in the object could be magnified by a large amount. Since the system is linear each point in the object will be convolved with a scaled image of the source point and then projected onto the detector line.

5.2 Noise in Reconstructed Images

We will now consider the effect of noise in the projection data on a reconstructed image. There are two types of noise to be considered. The first, a continuously varying error due to electrical noise or roundoff errors, can be modeled as a simple additive noise. The reconstructed image can therefore be considered to be the sum of two images, the true image and that image resulting from the noise. The second type of noise is best exemplified by shot noise in x-ray tomography. In this case the magnitude of the possible error is a function of the number of x-ray photons that exit the object and the error analysis becomes more involved.

Fig. 5.10: *The ray paths for normal and quarter offset detectors are compared here. Each ray path is represented by plotting an asterisk at the point on the ray closest to the origin. In each case 6 projections of 10 rays each were gathered by rotating a full 360° around the object. (Note: normally only 180° of projection data is used for parallel projection reconstruction.) (a) shows parallel projections without quarter offset (note that the extra 180° of data is redundant). (b) is identical to (a) but the detector array has been shifted by a quarter of the sampling interval. (c) shows equiangular projections without quarter offset and (d) is identical to (c) but the detector array has been shifted by a quarter of the sampling interval.*

5.2.1 The Continuous Case

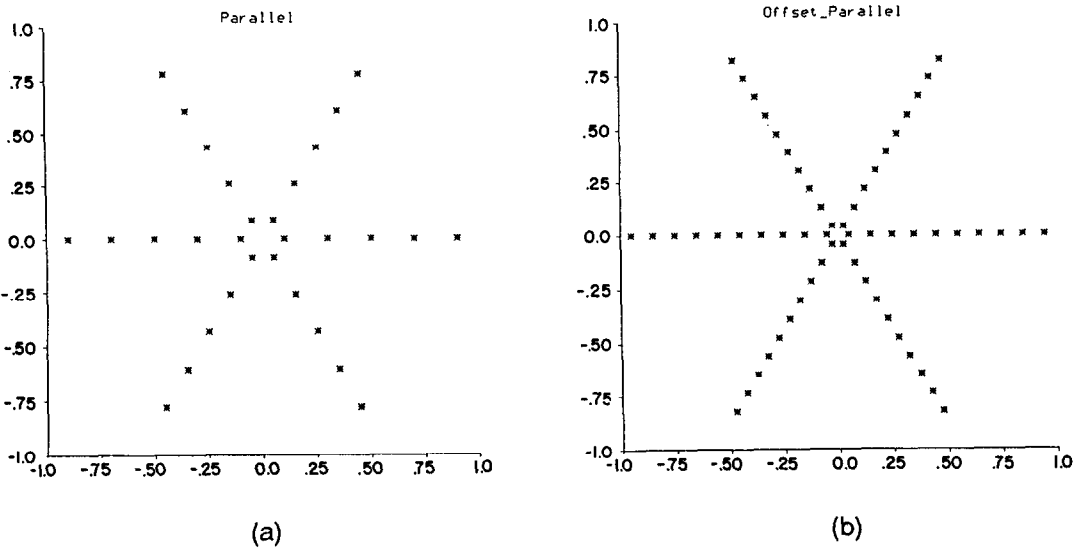
Consider the case where each projection, $P_\theta(t)$, is corrupted by additive noise $\nu_\theta(t)$. The measured projections, $P_\theta^m(t)$, are now given by

$$P_\theta^m(t) = P_\theta(t) + \nu_\theta(t). \quad (28)$$

We will assume that the noise is a stationary zero-mean random process and that its values are uncorrelated for any two rays in the system. Therefore,

$$E[\nu_{\theta_1}(t_1)\nu_{\theta_2}(t_2)] = S_0 \delta(\theta_1 - \theta_2)\delta(t_1 - t_2). \quad (29)$$

The reconstruction from the measured projection data is obtained by first



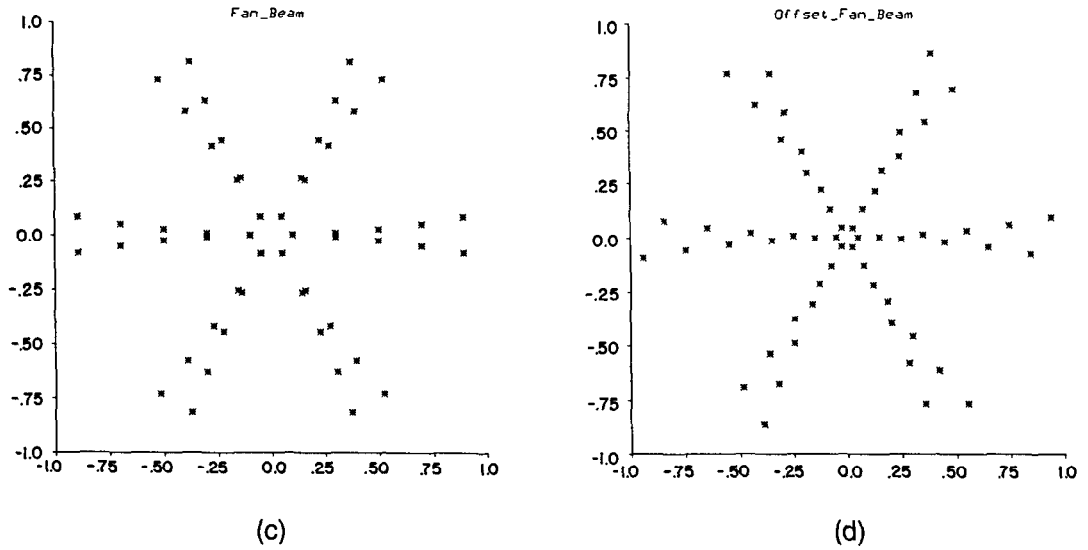


Fig. 5.10: Continued.

filtering each projection:

$$Q_{\theta}^m(t) = \int_{-\infty}^{\infty} S_{\theta}^m(w) |w| G(w) e^{j2\pi w t} dw \quad (30)$$

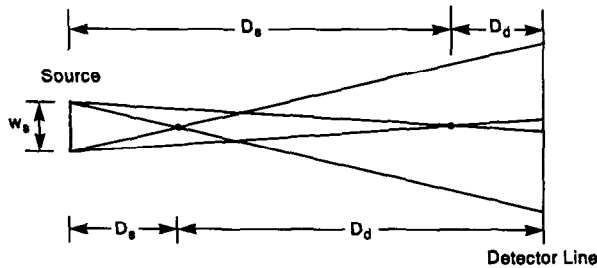
where $S_{\theta}^m(w)$ is the Fourier transform of $P_{\theta}^m(t)$ and $G(w)$ is the smoothing filter used; and then backprojecting the filtered projections:

$$\hat{f}(x, y) = \int_0^{\pi} Q_{\theta}^m(x \cos \theta + y \sin \theta) d\theta \quad (31)$$

where $\hat{f}(x, y)$ is the reconstructed approximation to the original image $f(x, y)$. For the purpose of noise calculations, we substitute (28) and (30) in (31) and write

$$\hat{f}(x, y) = \int_0^{\pi} \int_{-\infty}^{\infty} [S_{\theta}(w) + N_{\theta}(w)] |w| G(w) e^{j2\pi w(x \cos \theta + y \sin \theta)} dw d\theta \quad (32)$$

Fig. 5.11: A finite source of width w_s will be imaged by each point in the object onto the detector line. The size of the image will depend on the ratio of D_s to D_d . The images of two points in the object are shown here.



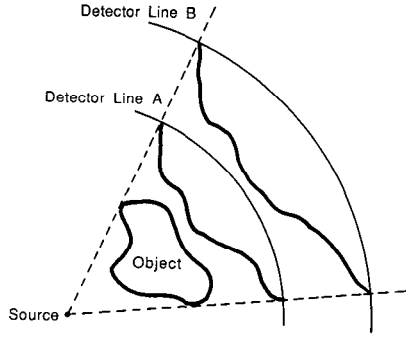


Fig. 5.12: The magnification of a projection due to a fan beam system is shown here. To find the effect of the source or detector aperture on image resolution it is necessary to map the blurring of the projection into an equivalent object size.

where, as before, $S_\theta(w)$ is the Fourier transform of the ideal projection $P_\theta(t)$, and $N_\theta(w)$ is the Fourier transform of the additive noise, $\nu_\theta(t)$. (Here we assume $N_\theta(w)$ exists in some sense. Note that in spite of our notation we are only dealing with projections with finite support.) Clearly,

$$N_\theta(w) = \int_{-\infty}^{\infty} \nu_\theta(t) e^{-j2\pi w t} dt \quad (33)$$

from which we can write

$$E[N_{\theta_1}(w_1)N_{\theta_2}^*(w_2)] = \int_{-\infty}^{\infty} \int_{-\infty}^{\infty} E[\nu_{\theta_1}(t_1)\nu_{\theta_2}^*(t_2)] e^{-j2\pi(w_1 t_1 - w_2 t_2)} dt_1 dt_2 \quad (34)$$

$$= S_0 \delta(w_1 - w_2) \delta(\theta_1 - \theta_2) \quad (35)$$

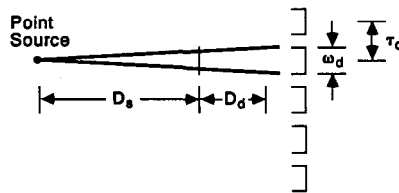
where we have used (29).

Since $N_\theta(w)$ is random, the reconstructed image given by (32) is also random. The mean value of $\hat{f}(x, y)$ is given by

$$E[\hat{f}(x, y)] = \int_0^\pi \int_{-\infty}^{\infty} [S_\theta(w) + E(N_\theta(w))] |w| G(w) e^{j2\pi w(x \cos \theta + y \sin \theta)} dw d\theta. \quad (36)$$

Fig. 5.13: A finite detector aperture leads to a blurring of the object.

Since we are dealing with zero-mean noise, $E[\nu_\theta(t)] = 0$; hence, from (33)



we get $E[N_\theta(w)] = 0$. Substituting this in (36), we get

$$E[\hat{f}(x, y)] = \int_0^\pi \int_{-\infty}^\infty S_\theta(w) |w| G(w) e^{j2\pi w(x \cos \theta + y \sin \theta)} dw d\theta. \quad (37)$$

Now the variance of noise at a point (x, y) in the reconstructed image is given by

$$\sigma_{\text{recon}}^2(x, y) = E[\hat{f}(x, y) - E(\hat{f}(x, y))]^2. \quad (38)$$

Substituting (32) and (37), we get

$$\sigma_{\text{recon}}^2(x, y) = E \left| \int_0^\pi \int_{-\infty}^\infty N_\theta(w) |w| G(w) e^{j2\pi w(x \cos \theta + y \sin \theta)} dw d\theta \right|^2 \quad (39)$$

$$= E \left[\int_0^\pi \int_{-\infty}^\infty N_\theta(w) |w| G(w) e^{j2\pi w(x \cos \theta + y \sin \theta)} dw d\theta \right]$$

$$\times \left[\int_0^\pi \int_{-\infty}^\infty N_\theta(w) |w| G(w) e^{j2\pi w(x \cos \theta + y \sin \theta)} dw d\theta \right]^* \quad (40)$$

$$= \pi S_0 \int_{-\infty}^\infty |w|^2 |G(w)|^2 dw \quad (41)$$

where we have used (35). Therefore, we may write

$$\frac{\sigma_{\text{recon}}^2}{S_0} = \pi \int_{-\infty}^\infty |w|^2 |G(w)|^2 dw \quad (42)$$

where we have dropped the (x, y) dependence of σ_{recon}^2 since it has turned out to be independent of position in the picture plane.

Equation (42) says that in order to reduce the variance of noise in a reconstructed image, the filter function $G(w)$ must be chosen such that the area under the square of $|w|G(w)$ is as small as possible. But note that if there is to be no image distortion $|w|G(w)$ must be as close to $|w|$ as possible. Therefore, the choice of $G(w)$ depends upon the desired trade-off between image distortion and noise variance.

We will conclude this subsection by presenting a brief description of the spectral density of noise in a reconstructed image. To keep our presentation simple we will assume that the projections consist only of zero-mean white noise, $\nu_\theta(t)$. The reconstructed image from the noise projections is given by

$$\hat{f}(x, y) = \int_0^\pi \int_{-\infty}^\infty N_\theta(w) |w| G(w) e^{j2\pi w(x \cos \theta + y \sin \theta)} dw d\theta \quad (43)$$

$$= \int_0^{2\pi} \int_0^\infty N_\theta(w) w G(w) e^{j2\pi w(x \cos \theta + y \sin \theta)} dw d\theta \quad (44)$$

where, as before, $N_\theta(w)$ is the Fourier transform of $\nu_\theta(t)$. Now let $R(\alpha, \beta)$ be the autocorrelation function of the reconstructed image:

$$R(\alpha, \beta) \equiv E[\hat{f}(x + \alpha, y + \beta)\hat{f}(x, y)] = E[\hat{f}(x + \alpha, y + \beta)\hat{f}^*(x, y)] \quad (45)$$

$$= S_0 \int_0^{2\pi} d\theta \int_0^\infty dw w^2 |g(w)|^2 e^{j2\pi w(\alpha \cos \theta + \beta \sin \theta)}. \quad (46)$$

From this one can show that the spectral density of the reconstructed noise is dependent only on the distance from the origin in the frequency domain and is given by

$$S_\nu(w, \theta) = S_0 |G(w)|^2 w \quad \text{and} \quad \begin{matrix} w \geq 0 \\ 0 < \theta \leq 2\pi \end{matrix} \quad (47)$$

where, of course, w is always positive. This may be shown by first expressing the result for the autocorrelation function in polar coordinates

$$R(r, \phi) = S_0 \int_0^\pi d\theta \int_0^\infty dw w^2 |G(w)|^2 e^{j2\pi wr \cos(\theta - \phi)} \quad (48)$$

$$= S_0 \int_0^\infty w |G(w)|^2 w J_0(2\pi wr) dw \quad (49)$$

and recognizing the Hankel transform relationship between the autocorrelation function and the spectral density given above.

5.2.2 The Discrete Case

Although the continuous case does bring out the dependence of the noise variance in the reconstructed image on the filter used for the projection data, it is based on a somewhat unrealistic assumption. The assumption of stationarity which led to (29) implies that in any projection the variance of measurement noise for each ray is the same. This is almost never true in practice. The variance of noise is often signal dependent and this has an important bearing on the structure of noise in the reconstructed image.

As an illustration of the case of signal-dependent noise consider the case of x-ray computerized tomography. Let τ be the sampling interval and also the width of the x-ray beam, as illustrated in Fig. 5.14. If the width τ of the beam is small enough and the beam is monochromatic the integral of the attenuation function $\mu(x, y)$ along line AB in Fig. 5.14 is given by

$$P_\theta(t) \equiv \int_{\text{ray path } AB} \mu(x, y) ds \approx \ln N_{\text{in}} - \ln N_\theta(k\tau) \quad (50)$$

where $N_\theta(k\tau)$ denotes the value of N_d for the ray at location $(\theta, k\tau)$ as shown in the figure. Randomness in the measurement of $P_\theta(t)$ is introduced by statistical fluctuations in $N_\theta(k\tau)$. Note that in practice only $N_\theta(k\tau)$ is

$$P_{\theta}(k\tau) = \int_{\text{ray path AB}} \mu(x, y) ds = \lambda n \frac{N_{in}}{N_d}$$

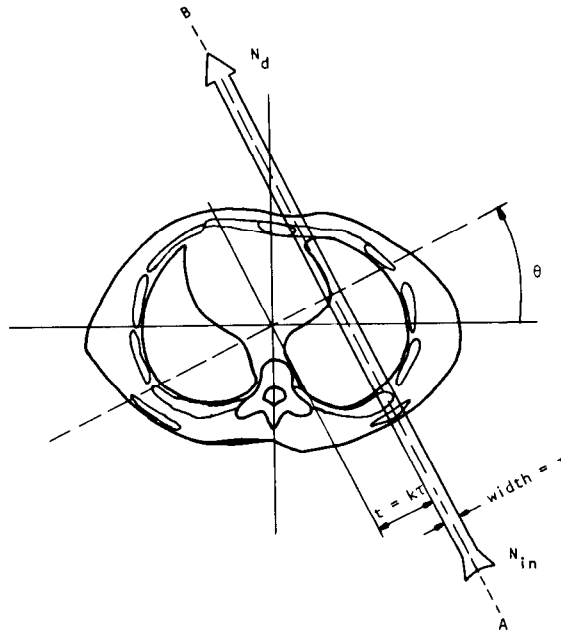


Fig. 5.14: An x-ray beam with a width of τ is shown traveling through a cross section of the human body. (From [Kak79].)

measured directly. The value of N_{in} for all rays is inferred by monitoring the x-ray source with a reference detector and from the knowledge of the spatial distribution of emitted x-rays. It is usually safe to assume that the reference x-ray flux is large enough so that N_{in} may be considered to be known with negligible error. In the rest of the discussion here we will assume that for each ray integral measurement N_{in} is a known deterministic constant, while on the other hand the directly measured quantity $N_{\theta}(k\tau)$ is a random variable. The randomness of $N_{\theta}(k\tau)$ is statistically described by the Poisson probability function [Ter67], [Pap65]:

$$p\{N_{\theta}(k\tau)\} = \frac{[\bar{N}_{\theta}(k\tau)]^{N_{\theta}(k\tau)}}{N_{\theta}(k\tau)!} e^{-\bar{N}_{\theta}(k\tau)} \quad (51)$$

where $p\{\cdot\}$ denotes the probability and $\bar{N}_{\theta}(k\tau)$ the expected value of the measurement:

$$\bar{N}_{\theta}(k\tau) = E\{N_{\theta}(k\tau)\} \quad (52)$$

where $E\{\cdot\}$ denotes statistical expectation. Note that the variance of each measurement is given by

$$\text{variance}\{N_{\theta}(k\tau)\} = \bar{N}_{\theta}(k\tau). \quad (53)$$

Because of the randomness in $N_\theta(k\tau)$ the true value of $P_\theta(k\tau)$ will differ from its measured value which will be denoted by $P_\theta^m(k\tau)$. To bring out this distinction we reexpress (50) as follows:

$$P_\theta^m(k\tau) = \ln N_{\text{in}} - \ln N_\theta(k\tau) \quad (54)$$

and

$$P_\theta(k\tau) = \int_{\text{ray}} \mu(x, y) ds. \quad (55)$$

By interpreting $e^{-P_\theta(k\tau)}$ as the probability that (along a ray such as the one shown in Chapter 4) a photon entering the object from side A will emerge (without scattering or absorption) at side B , one can show that

$$\tilde{N}_\theta(k\tau) = N_{\text{in}} e^{-P_\theta(k\tau)}. \quad (56)$$

We will now assume that all fluctuations (departures from the mean) in $N_\theta(k\tau)$ that have a significant probability of occurrence are much less than the mean. With this assumption and using (50) and (51) it is easily shown that

$$E\{P_\theta^m(k\tau)\} = P_\theta(k\tau) \quad (57)$$

and

$$\text{variance}\{P_\theta^m(k\tau)\} = \frac{1}{\tilde{N}_\theta(k\tau)}. \quad (58)$$

From the statistical properties of the measured projections, $P_\theta^m(k\tau)$, we will now derive those of the reconstructed image. Using the discrete filtered backprojection algorithms of Chapter 3, the relationship between the reconstruction at a point (x, y) and the *measured* projections is given by

$$\hat{f}(x, y) = \frac{\pi\tau}{M_{\text{proj}}} \sum_{i=1}^{M_{\text{proj}}} \sum_k P_{\theta_i}^m(k\tau) h(x \cos \theta_i + y \sin \theta_i - k\tau). \quad (59)$$

Using (57), (58), and (59), we get

$$E\{\hat{f}(x, y)\} = \frac{\pi\tau}{M_{\text{proj}}} \sum_{i=1}^{M_{\text{proj}}} \sum_k P_{\theta_i}(k\tau) h(x \cos \theta_i + y \sin \theta_i - k\tau) \quad (60)$$

and

$$\text{variance}\{\hat{f}(x, y)\} = \left(\frac{\pi\tau}{M_{\text{proj}}}\right)^2 \sum_i \sum_k \frac{1}{\tilde{N}_{\theta_i}(k\tau)} h^2(x \cos \theta_i + y \sin \theta_i - k\tau) \quad (61)$$

where we have used the assumption that fluctuations in $P_{\theta_i}^m(k\tau)$ are uncorrelated for different rays. Equation (60) shows that the expected value of the reconstructed image is equal to that made from the ideal projection data. Before we interpret (61) we will rewrite it as follows. In terms of the ideal projections, $P_{\theta}(k\tau)$, we define new projections as

$$V_{\theta}(k\tau) = e^{P_{\theta}(k\tau)} \quad (62)$$

and a new filter function, $h_v(t)$, as

$$h_v(t) = h^2(t). \quad (63)$$

Substituting (56), (62), and (63) in (61), we get

$$\text{variance } \{\hat{f}(x, y)\} = \left(\frac{\pi\tau}{M_{\text{proj}}}\right)^2 \frac{1}{N_{\text{in}}} \sum_i \sum_k V_{\theta}(k\tau) \cdot h_v(x \cos \theta_i + y \sin \theta_i - k\tau). \quad (64)$$

We will now define a *relative-uncertainty image* as follows¹:

$$\text{relative-uncertainty at } (x, y) = N_{\text{in}} \frac{\text{variance } \{\hat{f}(x, y)\}}{[\hat{f}(x, y)]^2}. \quad (65)$$

In computer simulation studies with this definition the relative-uncertainty image becomes independent of the number of incident photons used for measurements, and is completely determined by the choice of the phantom. Fig. 5.15(c) shows the relative-uncertainty image for the Shepp and Logan phantom (Fig. 5.15(b)) for $M_{\text{proj}} = 120$ and $\tau = 2/101$ and for $h(t)$ originally described in Chapter 3. Fig. 5.15(d) shows graphically the middle horizontal line through Fig. 5.15(c). The relative-uncertainty at (x, y) gives us a measure of how much confidence an observer might place in the reconstructed value at the point (x, y) vis-à-vis those elsewhere.

We will now derive some special cases of (64). Suppose we want to determine the variance of noise at the origin. From (64) we can write

$$\text{variance } \{\hat{f}(0, 0)\} = \left(\frac{\pi\tau}{M_{\text{proj}}}\right)^2 \sum_{i=1}^{M_{\text{proj}}} \sum_k \frac{1}{\bar{N}_{\theta_i}(k\tau)} h^2(k\tau) \quad (66)$$

where we have used the fact that $h(t)$ is an even function. Chesler *et al.* [Che77] have argued that since $h(k\tau)$ drops rapidly with k (see Chapter 3), it is safe to make the following approximation for objects that are approxi-

¹ This result only applies when compensators aren't used to reduce the dynamic range of the detector output signal. In noise analyses their effect can be approximately modeled by using different N_{in} 's for different rays.

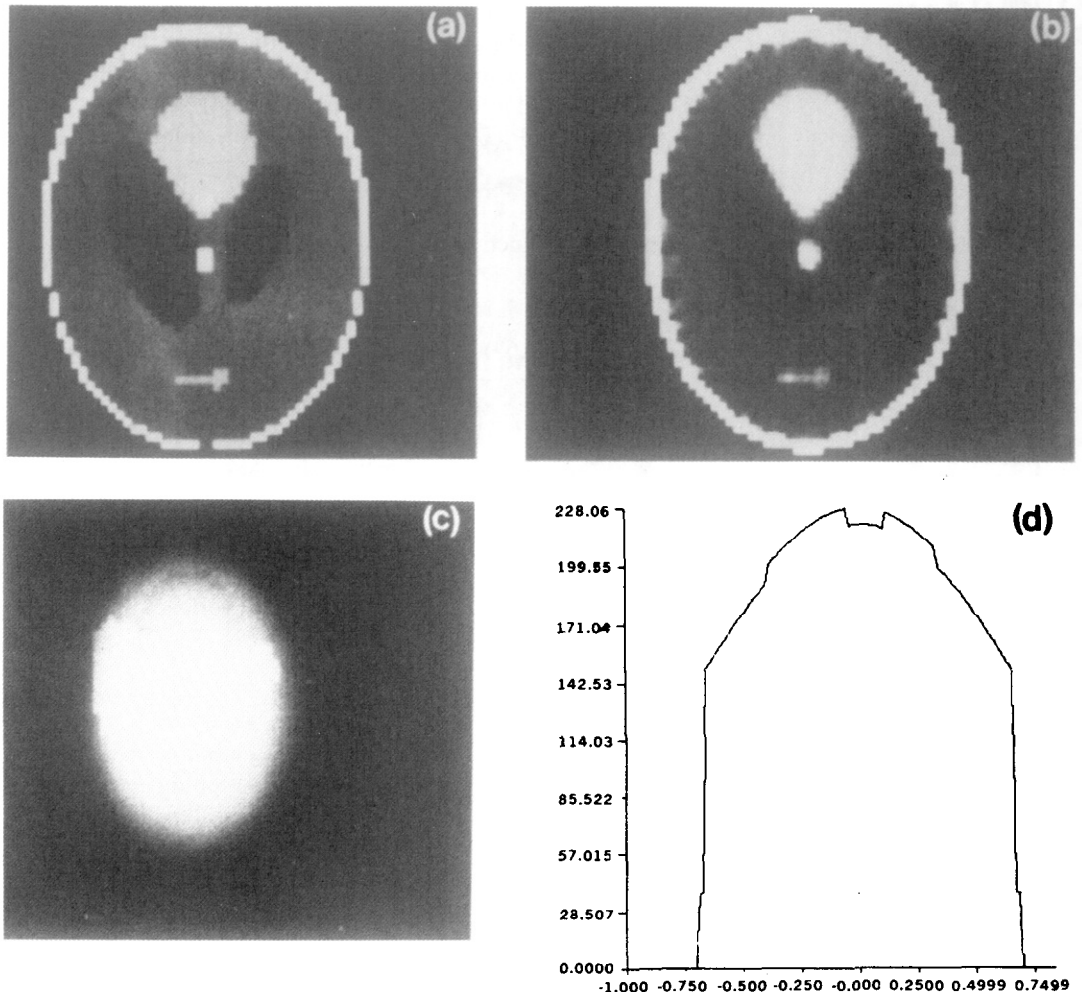


Fig. 5.15: (a) A Shepp and Logan head phantom [She74] is shown here. (b) A reconstruction of the phantom from 120 projections and 101 rays in each parallel projection. The display matrix was 64×64 . (c) The relative-uncertainty image for the reconstruction in (b). (d) A graphic depiction of the relative-uncertainty values through the middle horizontal line of (c). (From [Kak79].)

mately homogeneous:

$$\text{variance } \{ \hat{f}(0, 0) \} = \left(\frac{\pi \tau}{M_{\text{proj}}} \right)^2 \sum_k h^2(k\tau) \sum_{i=1}^{M_{\text{proj}}} \frac{1}{\bar{N}_{\theta_i}(0)} \quad (67)$$

which, when τ is small enough, may also be written as

$$\text{variance } \{ \hat{f}(0, 0) \} = \left(\frac{\pi}{M_{\text{proj}}} \right)^2 \tau \int_{-\infty}^{\infty} h^2(t) dt \sum_{i=1}^{M_{\text{proj}}} \frac{1}{\bar{N}_{\theta_i}(0)}. \quad (68)$$

Note again that the $\bar{N}_{\theta_i}(0)$ are the mean number of exiting photons measured for the center ray in each projection. Using (68) Chesler *et al.* [Che77] have arrived at the very interesting result that (for the same uncertainty in measurement) the total number of photons per resolution element required for x-ray CT (using the filtered backprojection algorithm) is the same as that required for the measurement of attenuation of an isolated (excised) piece of the object with dimensions equal to those of the resolution element.

Now consider the case where the cross section for which the CT image is being reconstructed is circularly symmetric. The $\bar{N}_{\theta_i}(0)$'s for all i 's will be equal; call their common value \bar{N}_0 . That is, let

$$\bar{N}_0 = \bar{N}_{\theta_1}(0) = \bar{N}_{\theta_2}(0) = \dots \quad (69)$$

The expression (68) for the variance may now be written as

$$\text{variance } \{ \hat{f}(0, 0) \} = \frac{\pi^2 \tau}{M_{\text{proj}} \bar{N}_0} \int_{-\infty}^{\infty} h^2(t) dt. \quad (70)$$

By Parseval's theorem this result may be expressed in the frequency domain as

$$\text{variance } \{ \hat{f}(0, 0) \} = \frac{\pi^2 \tau}{M_{\text{proj}} \bar{N}_0} \int_{-1/2\tau}^{1/2\tau} |H(w)|^2 dw \quad (71)$$

where τ is the sampling interval for the projection data. This result says that the variance of noise at the origin is proportional to the area under the square of the filter function used for reconstruction. This doesn't imply that this area could be made arbitrarily small since any major departure from the $|w|$ function will introduce spatial distortion in the image even though it may be less noisy. *None of the equations above should be construed to imply that the signal-to-noise ratio approaches zero as τ is made arbitrarily small.* Note from Chapter 4 that τ is also the width of the measurement beam. In any practical system, as τ is reduced \bar{N}_0 will decrease also.

The preceding discussion has resulted in expressions for the variance of noise in reconstructions made with a filtered backprojection algorithm for parallel projection data. As mentioned before, filtered backprojection algorithms have become very popular because of their accuracy. Still, given a set of projections, can there be an algorithm that might reconstruct an image with a smaller error? The answer to this question has been supplied by Tretiak [Tre78]. Tretiak has derived an algorithm-independent lower bound for the mean squared error in a reconstructed image and has argued that for the case of reconstructions from parallel projection data this lower bound is very close to the error estimates obtained by Brooks and DiChiro [Bro76] for the filtered backprojection algorithms, which leads to the conclusion that very little improvement can be obtained over the performance of such an algorithm.

5.3 Bibliographic Notes

Aliasing artifacts in tomographic imaging with nondiffracting sources have been studied by Brooks *et al.* [Bro78], [Bro79] and Crawford and Kak [Cra79]. A different analysis of the optimum number of rays and projections was presented in [Sch77] and reached nearly the same conclusion. A more detailed analysis is in [Jos80]. Excellent work describing the effects of sampling on CT images has been published in [Jos80], [Jos80b], [Bro79].

With regard to the properties of noise in images reconstructed with filtered backprojection, Shepp and Logan [She74] first showed that when filtered backprojection algorithms are used, the variance of the noise is directly proportional to the area under the square of the filter function. This derivation was based on the assumption that the variance of the measurement noise is the same for all the rays in the projection data, a condition which is usually not satisfied. The variance of the reconstruction was also studied by Gore and Tofts [Gor78]. This assumption was also used by Riederer *et al.* [Rie78] to derive the spectral density of the noise in a CT reconstruction.

A more general expression (not using this assumption) for the noise variance was derived by Kak [Kak79] who has also introduced the concept of "the relative-uncertainty image." For tomographic imaging with x-rays, Tretiak [Tre78] has derived an algorithm-independent lower bound on the noise variance in a reconstructed image. An explanation of the trade-offs between reconstruction noise in x-ray CT and image resolution is given in [Che77], [Alv79], [Kow77].

5.4 References

- [Alv79] R. E. Alvarez and J. P. Stonestrom, "Optimal processing of computed tomography images using experimentally measured noise properties," *J. Comput. Tomog.*, vol. 3, no. 1, pp. 77-84, 1979.
- [Bro76] R. A. Brooks and G. DiChiro, "Statistical limitations in x-ray reconstructive tomography," *Med. Phys.*, vol. 3, pp. 237-240, 1976.
- [Bro78] R. A. Brooks, G. H. Weiss, and A. J. Talbert, "A new approach to interpolation in computed tomography," *J. Comput. Assist. Tomog.*, vol. 2, pp. 577-585, Nov. 1978.
- [Bro79] R. A. Brooks, G. H. Glover, A. J. Talbert, R. L. Eisner, and F. A. DiBianca, "Aliasing: A source of streaks in computed tomograms," *J. Comput. Assist. Tomog.*, vol. 3, no. 4, pp. 511-518, Aug. 1979.
- [Che77] D. A. Chesler, S. J. Riederer, and N. J. Pelc, "Noise due to photon counting statistics in computed x-ray tomography," *J. Comput. Assist. Tomog.*, vol. 1, pp. 64-74, Jan. 1977.
- [Cra79] C. R. Crawford and A. C. Kak, "Aliasing artifacts in computerized tomography," *Appl. Opt.*, vol. 18, pp. 3704-3711, 1979.
- [Gor78] J. C. Gore and P. S. Tofts, "Statistical limitations in computed tomography," *Phys. Med. Biol.*, vol. 23, pp. 1176-1182, 1978.
- [Jos80a] P. M. Joseph, "The influence of gantry geometry on aliasing and other geometry dependent errors," *IEEE Trans. Nucl. Sci.*, vol. 27, pp. 1104-1111, 1980.
- [Jos80b] P. M. Joseph, R. D. Spital, and C. D. Stockham, "The effects of sampling on CT images," *Comput. Tomog.*, vol. 4, pp. 189-206, 1980.
- [Jos80] P. M. Joseph and R. A. Schulz, "View sampling requirements in fan beam computed tomography," *Med. Phys.*, vol. 7, no. 6, pp. 692-702, Nov./Dec. 1980.

- [Kak79] A. C. Kak, "Computerized tomography with x-ray emission and ultrasound sources," *Proc. IEEE*, vol. 67, pp. 1245-1272, 1979.
- [Kak84] —, "Image reconstruction from projections," in *Digital Image Processing Techniques*, M. P. Ekstrom, Ed. New York, NY: Academic Press, 1984.
- [Kow77] G. Kowalski, "Reconstruction of objects from their projections. The influence of measurement errors on the reconstruction," *IEEE Trans. Nucl. Sci.*, vol. NS-24, pp. 850-864, Feb. 1977.
- [Pap65] A. Papoulis, *Probability, Random Variables, and Stochastic Processes*. New York, NY: McGraw-Hill, 1965 (2nd ed., 1984).
- [Rie78] S. J. Riederer, N. J. Pelc, and D. A. Chesler, "The noise power spectrum in computer x-ray tomography," *Phys. Med. Biol.*, vol. 23, pp. 446-454, 1978.
- [Ros82] A. Rosenfeld and A. C. Kak, *Digital Picture Processing*, 2nd ed. New York, NY: Academic Press, 1982.
- [Sch77] R. A. Schulz, E. C. Olson, and K. S. Han, "A comparison of the number of rays vs the number of views in reconstruction tomography," *SPIE Conf. on Optical Instrumentation in Medicine VI*, vol. 127, pp. 313-320, 1977.
- [She74] L. A. Shepp and B. F. Logan, "The Fourier reconstruction of a head section," *IEEE Trans. Nucl. Sci.*, vol. NS-21, pp. 21-43, 1974.
- [Ter67] M. TerPogossian, *The Physical Aspects of Diagnostic Radiology*. New York, NY: Harper and Row, 1967.
- [Tre78] O. J. Tretiak, "Noise limitations in x-ray computed tomography," *J. Comput. Assist. Tomog.*, vol. 2, pp. 477-480, Sept. 1978.